Manuscript submitted to: Volume 3, Issue 1, 121-143.

AIMS Energy DOI: 10.3934/energy.2015.1.121

Received date 17 December 2014, Accepted date 9 February 2015, Published date 27 February 2015

Review

Nanostructured, complex hydride systems for hydrogen generation

Robert A. Varin * and Amirreza Shirani Bidabadi

Department of Mechanical and Mechatronics Engineering, University of Waterloo, 200 University Ave. W., Waterloo, Ontario, Canada N2L 3G1

*** Correspondence:** Email: robert.varin@uwaterloo.ca; Tel: +1-519-888-4567; Fax: +1-519-885-5862.

Abstract: Complex hydride systems for hydrogen (H_2) generation for supplying fuel cells are being reviewed. In the first group, the hydride systems that are capable of generating H_2 through a mechanical dehydrogenation phenomenon at the ambient temperature are discussed. There are few quite diverse systems in this group such as lithium alanate ($LiAlH_4$) with the following additives: nanoiron (n-Fe), lithium amide ($LiNH_2$) (a hydride/hydride system) and manganese chloride $MnCl_2$ (a hydride/halide system). Another hydride/hydride system consists of lithium amide ($LiNH_2$) and magnesium hydride (MgH_2), and finally, there is a $LiBH_4$-$FeCl_2$ (hydride/halide) system. These hydride systems are capable of releasing from ~4 to 7 wt.% H_2 at the ambient temperature during a reasonably short duration of ball milling. The second group encompasses systems that generate H_2 at slightly elevated temperature (up to 100 °C). In this group lithium alanate ($LiAlH_4$) ball milled with the nano-Fe and nano-TiN/TiC/ZrC additives is a prominent system that can relatively quickly generate up to 7 wt.% H_2 at 100 °C. The other hydride is manganese borohydride ($Mn(BH_4)_2$) obtained by mechano-chemical activation synthesis (MCAS). In a ball milled ($2LiBH_4 + MnCl_2$) nanocomposite, $Mn(BH_4)_2$ co-existing with LiCl can desorb ~4.5 wt.% H_2 at 100 °C within a reasonable duration of dehydrogenation. Practical application aspects of hydride systems for H_2 generation/storage are also briefly discussed.

Keywords: hydrogen generation; mechano-chemical activation synthesis; mechanical dehydrogenation; thermal dehydrogenation

1. Introduction

A major challenge for this century is the transition from the economy based on fossil fuels to the sustainable and environmentally friendly economy based on renewable and clean resources which must be developed to meet the increasing energy demands of the world [1,2]. Hydrogen (H_2) has been

suggested as a principal, potential future energy carrier which would eventually lead to the implementation of the world-wide Hydrogen Economy [1,2]. That decisive shift would be allowed by applying hydrogen (H_2) in a great variety of industrial and commercial applications.

In the transitional stage of transformation from the fossil fuels energy to hydrogen energy supply, a wide usage of fuel cells (FC) where hydrogen gas (H_2) in contact with oxygen (O_2) is converted into an electrical energy, must become a widespread reality. Furthermore, finding effective hydrogen storage systems for supplying FCs is another most important issue. There are three possible storage/generation systems for supplying H_2 to a FC stack: gaseous H_2, liquid H_2 or solid hydrides. A mass transportation using cars (automotive) is the most important area where a fast transformation from fossil fuels to hydrogen would be most beneficial. For the automotive sector, solid state hydrogen storage in hydrides could be advantageous over gas and liquid storage because most solid hydrides exhibit a higher H_2 volumetric density than gas or liquid storage [3–6]. In addition, such serious safety problems like a very high pressure of 70 MPa for H_2 gas storage or large thermal losses for liquid H_2, which requires a formidable insulation and an open storage system [3–6], could be eliminated. In addition, substantial pressurization or liquefaction costs could be avoided.

However, solid state H_2 storage in hydrides has its own serious constraints. First, reaction of H_2 and oxygen (O_2) in a commercial high power density Proton Exchange Membrane fuel cell (PEM FC) (sometimes also named a Polymer Electrolyte Fuel Cell (PEFC)) imposes important constraints on solid hydrides for potential H_2 storage. A large PEM FC stack (a few hundred cells) generates the quantity of waste heat which is able to rise coolant temperature to 70–80 °C. Second, a PEM FC operates at H_2 fuel pressure slightly above 1 bar (usually 1.1–1.8 bar). Therefore, the suitable solid hydrides for generating H_2 gas should rapidly desorb H_2 under pressure levels roughly 1.0–1.8 bar and at low temperatures, not exceeding the waste heat temperature of a FC stack (60–80 °C) which, in turn, could be used for heating a hydride storage tank to release H_2. Therefore, for the preliminary, experimental screening of hydrides, the hydride systems that are of potential interest for solid state hydrogen storage, including automotive applications, are only those that would desorb H_2 under at least 1 bar H_2 pressure (or slightly higher) and at temperatures not exceeding approximately 100 °C.

The second constraint is a requirement for a reasonable driving distance. The US Department of Energy target for 2017 is 5.5 wt.% H_2 for the entire fuel system [7] to drive 300 miles (480 km), which roughly corresponds to at least 10–11 wt.% H_2 necessary capacity for the desorbing material/hydride. Furthermore, the potential automotive solid state hydride storage systems would have to be easily reversible by allowing "on board" rehydrogenation under medium H_2 pressures, at a charging time not exceeding approximately 3.3 min [7] and within a temperature range not exceeding the waste heat temperature of a FC stack (70–80 °C). Unfortunately, despite enormous research efforts in the past 15 years a high capacity hydride storage system specifically suited for an automotive market is still very elusive and there is a growing doubt if it would ever be found [5,6,8]. Since the automotive solid state H_2 storage is still very futuristic, the first commercial Toyota and Hyundai Fuel Cell Vehicles (FCV), coming to market in 2015–2016 [9,10] will store H_2 in a more conventional, gaseous form under a high pressure of 70 MPa.

However, there is a number of other potential market applications for H_2 generation systems at ambient and slightly elevated temperatures. Those H_2 systems became available in the past years by novel processing and synthesis methods, that could enhance a gradual implementation of the Hydrogen Economy in the commercial, non-automotive sectors of the economy. They could be utilized in such applications as, for example, portable electronic devices, stationary auxiliary power

systems, off-road vehicles, lawn mowers, air transportation, coastal and international shipping, bulk hydrogen storage and many others which will be discussed in more detail later on.

The present review focuses on the results obtained hitherto in our laboratory in the past few years on various types of solid hydride H_2 generators of principally non-automotive character. These hydride systems have been synthesized by controlled ball milling under varying energy levels using the magneto-mill Uni-ball Mill 5 [11–13] resulting in some novel hydrides formed by mechano-chemical activation synthesis (MCAS) involving metathesis or, in other words, double substitution reactions. The microstructure and properties for hydrogen generation of these novel systems will be discussed. The experimental details of the processing have already been published in a number of publications and will not be repeated in the present work. Readers are encouraged to refer to the original publications. It must be pointed out that ball milling leads to the formation of nanostructure in the hydride systems. Either powder nanoparticles or crystallites (nanograins) within the larger powder particles are being formed during ball milling [3]. These aspects of microstructure will also be discussed for each hydride system described here wherever possible. Since in the presented hydride systems either additives or hydrides are nanometric we will use a term "nanocomposite". Finally, for clarity, the quantities of wt.% H_2 released which are reported in the present work are always referred to *the whole mass of the solid powder,* i.e. hydride with all additives.

2. Hydrogen Generators Through Mechanical Dehydrogenation at the Ambient Temperature

2.1. $LiAlH_4$ with various additives

Recently, we have found that the lithium alanate ($LiAlH_4$) hydride, ball milled together with the nano-iron (n-Fe) particles additive (average particle size d50 < 50 nm; specific surface area (SSA) ~25 m^2/g) under a high energy milling mode starts decomposing rapidly during milling, releasing large quantities of H_2 (Figure 1a) up to about 3.5 wt.% after 5 h (300 min) of ball milling [4,14]. This is a typical phenomenon of "mechanical dehydrogenation" that will be also shown and discussed for $LiAlH_4$ mixed with other additives and complex borohydride systems. An enhanced mechanical dehydrogenation has never been reported for the n-Fe additive to $LiAlH_4$. It must be stressed out that no H_2 desorption is observed during low energy milling of $LiAlH_4$ containing n-Fe under a low energy shearing mode (Figure 1a). Similarly, no H_2 desorption occurred during high energy ball milling for $LiAlH_4$ containing micrometric Fe (μ-Fe) and, for comparison, both the micrometric and nanometric Ni (μ-Ni and n-Ni) additive [4,14]. Figure 1b compares the XRD patterns obtained from the powders milled under a high energy mode for 15 min, 1 h and 5 h with the XRD pattern for just mixed powder. After only 15 min of milling the diffraction peaks of Li_3AlH_6 are clearly seen as opposed to the $LiAlH_4$ peaks observed for the mixed powders. The intensity of the Li_3AlH_6 peaks increases after 1 and 5 h of milling while the intensity of $LiAlH_4$ peaks gradually decreases and they eventually disappear (Figure 1b). Simultaneously, more H_2 is desorbed as can be seen in Figure 1a. It is obvious that during high energy milling there is a gradual decomposition of $LiAlH_4$ in solid state according to reaction described by Equation (1):

$$LiAlH_4(s) \rightarrow 1/3Li_3AlH_6(s)+2/3Al(s)+H_2(g) \quad (1)$$

where s-solid and g-gas. The theoretical H_2 capacity of this reaction is 5.3 wt.% H_2.

We have also found from X-ray diffraction that ball milling results in a varying degree of the lattice expansion of $LiAlH_4$ for both the nanometric Fe and Ni (n-Fe and n-Ni) additives as shown in Figure 2. It seems that a volumetric lattice expansion larger than 1% triggers the accelerated decomposition of $LiAlH_4$ accompanied by a continuous H_2 desorption during milling according to Equation (1). It is hypothesized that the Fe and Ni ions are able to dissolve in the lattice of $LiAlH_4$ by the combined action of mechanical energy and chemical reaction, forming a substitutional solid solution of either the $LiAlFe_xH_4$ or $LiAlNi_xH_4$ type [4,14]. The ionic radius of 77 pm for Fe^{2+} is much larger than 53 pm for Al^{3+} [15] and the $LiAlH_4$ lattice expansion increases. In contrast, the ionic radius of Ni^{2+} is 69 pm [15] and the volumetric lattice expansion is smaller (Figure 2). It is interesting that the profound dissolution of the Fe^{2+} ions in the $LiAlH_4$ matrix can only occur when the Fe additive is nanometric while it does not occur if the additive is micrometric in size [4,14]. Furthermore, the experimental results in Figure 2 show that n-Fe is more efficient in enhancing the dehydrogenation of $LiAlH_4$ during ball milling than n-Ni. This is a puzzling finding because the Ni^{2+} ionic radius is smaller than that of the Fe^{2+} ion and thus, one would expect more Ni^{2+} ions dissolved in the $LiAlH_4$ lattice. Apparently, for the same milling conditions, the incorporation of Ni^{2+} ions into the ionic-covalent crystal of $LiAlH_4$ is less efficient than the Fe^{2+} ions as can be seen in Figure 2. Therefore, it was suggested that an efficient incorporation of metal atoms/ions in the $LiAlH_4$ lattice could be driven by chemical reactions with use of oxide form of the alloying metal, instead of the metal itself [4,14]. Indeed, the received n-Fe (NANOFER 25S from the Nano Iron, s.r.o., The Czech Republic) contained Fe_3O_4 [4,14]. Finally, it must be pointed out that the mechanism of accelerated mechanical dehydrogenation of $LiAlH_4$ (Figure 1) seems not to be a typical catalytic mechanism in which a catalyst is supposed to boost the surface formation of molecular H_2 from the atomic hydrogen escaping from the bulk [3,4].

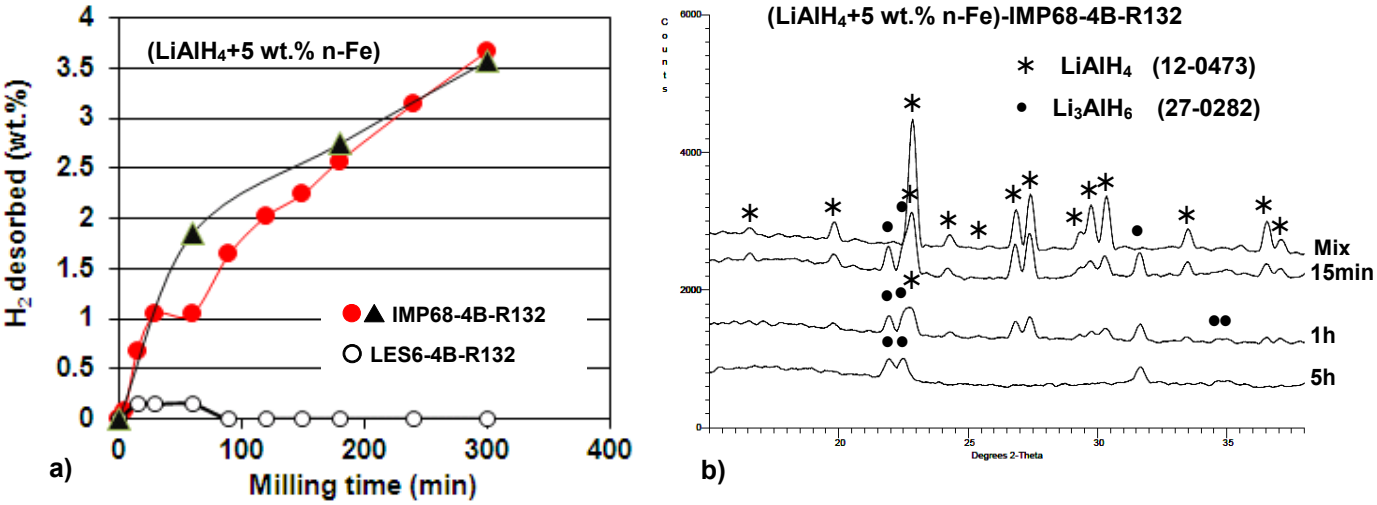

Figure 1. The quantity of H_2 desorbed in the process of mechanical dehydrogenation during ball milling under the high energy impact mode (IMP68) and the low energy shearing mode (LES6) as a function of milling time. Milling under high energy mode (IMP68) was repeated twice (solid circles and triangles). (b) XRD patterns after milling under the high energy (IMP68) mode for various times. ICDD file numbers are shown for peak identification. 4B-four balls in the milling vial. Ball-to-powder weight ratio R = 132 [4,14].

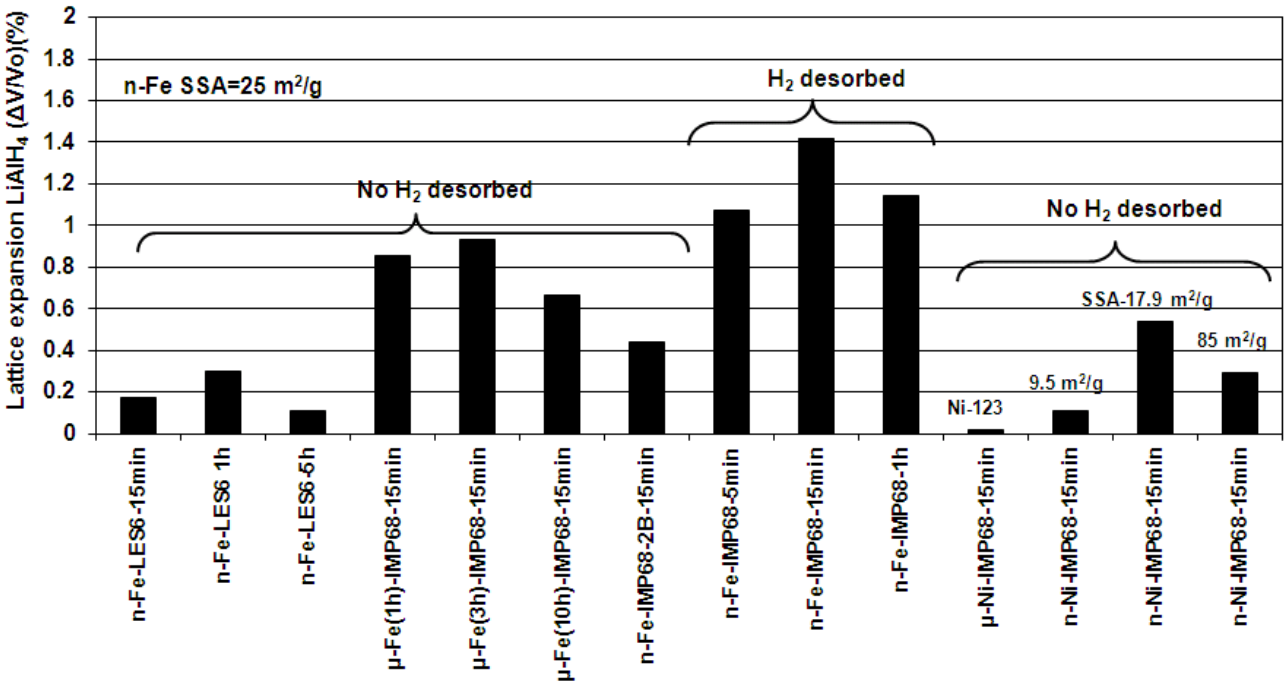

Figure 2. The correlation of the volumetric lattice expansion for $LiAlH_4$ with the type of Fe additive, micrometric (μ-Fe) and nanometric (n-Fe), milling mode and observed hydrogen desorption event during milling. For comparison, the results for μ-Ni and n-Ni are also shown. Milling conducted with four balls (4B) in the milling vial except where two balls (2B) are indicated; milling time duration is shown. Ball-to-powder weight ratio R = 132. IMP68-impact mode with two magnets, LES6-low energy shearing mode with one magnet. SSA-specific surface area. 1 h, 3 h and 10 h-indicate the length of pre-milling time for the micrometric Fe additive [4,14].

Another example of a rapid mechanical dehydrogenation of $LiAlH_4$ is the addition of 5 wt.% nanometric interstitial compounds such as n-TiC (average particle size 40 nm; specific surface area (SSA) = 50 m^2/g), n-TiN (average particle size 20 nm; SSA > 80 m^2/g) and n-ZrC (average particle size 40 nm; SSA > 70 m^2/g) [16]. The interstitial compounds are composed of the transition metals (T) with relatively large atomic radii with nonmetals having small radii (H, B, C, N and O) [17]. Figure 3 shows the quantity of H_2 desorbed during ball milling of $LiAlH_4$ containing 5 wt.% of the interstitial compound additive. After about 18 h of milling the amount of mechanical dehydrogenation for the n-TiN additive reaches ~6.6 wt.% H_2. Finally, after 25 h of milling mechanical dehydrogenation results in ~7 wt.% H_2 desorbed for the n-TiC additive, and ~3 wt.% H_2 for the n-ZrC additive. Therefore, the mechanical dehydrogenation curves in Figure 3 confirm that the mechanical dehydrogenation rate of the samples containing the interstitial compound additives increases noticeably during high energy ball milling with increasing quantity of injected energy in the order of n-TiN > n-TiC > n-ZrC. Since the maximum theoretical H_2 capacity of reaction Equation (1) is only 5.3 wt.% H_2 then desorption of ~7 wt.% H_2 during the mechanical dehydrogenation of $LiAlH_4$ with n-TiN and n-TiC requires another reaction to occur according to Equation (2) [3,4,16]:

$$1/3Li_3AlH_6 \rightarrow LiH + 1/3Al + 0.5H_2 \quad \text{(theoretical 2.6 wt.\% } H_2\text{)} \quad (2)$$

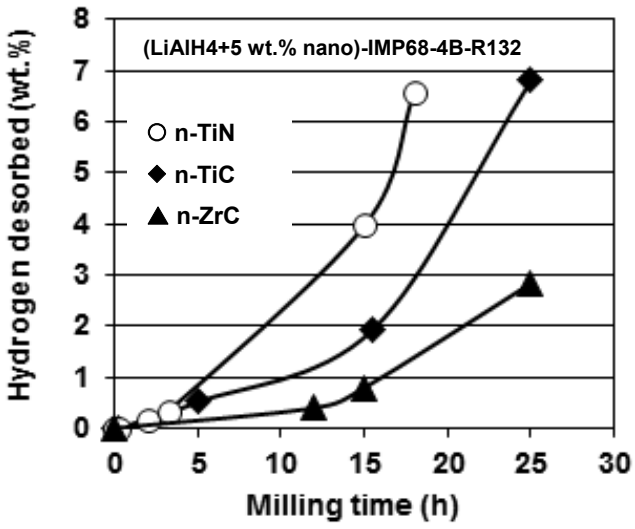

Figure 3. The quantity of H_2 desorbed during ball milling (mechanical dehydrogenation) under the high impact energy mode IMP68-4B-R132 as a function of milling time for $LiAlH_4$ containing 5 wt.% of nanometric TiC, TiN and ZrC [4,16].

The combined theoretical capacity for reactions described by Equation (1) and (2) is 7.9 wt. H_2 and the practical H_2 capacity is ~7.3 wt.% if both the purity and presence of 5 wt.% additive are taken into account (4.9 and 2.4 wt.% H_2 for reactions (1) and (2), respectively [16]). Figure 3 shows that nearly 55% of the maximum available H_2 capacity of the ($LiAlH_4$ + 5wt.% n-TiN) nanocomposite can be desorbed during milling up to 15 h, while the nanocomposites with 5 wt.% n-TiC and n-ZrC release almost 23% and 10% of their respective maximum available capacity after the same milling time, respectively. The upward trend of desorption curves in Figure 3 suggests that applying longer milling duration could, most likely, result in a total H_2 desorption from the catalyzed nanocomposites. The XRD measurements confirmed the correctness of reactions Equation (1) and (2) [16]. The examination of the XRD patterns after various ball milling durations also confirmed a continuous presence of well visible diffraction peaks of nanometric interstitial compounds. This observation provides strong evidence that they do not decompose during high energy ball milling and thus exhibit a considerable chemical stability. Furthermore, calculations of the unit cell volume of $LiAlH_4$ after ball milling showed no measurable change in the unit cell volume [16]. It is quite apparent that accelerated mechanical dehydrogenation for $LiAlH_4$ containing nanometric interstitial compounds in Figure 3 is unrelated to the lattice expansion that might have been induced by, for example, diffusion of the Ti or Zr ions from the nanometric interstitial compounds into the $LiAlH_4$ crystal lattice as shown earlier for the n-Fe additive. The absence of a measurable lattice expansion is in agreement with the experimental fact that the nanometric interstitial compounds are very stable during high energy ball milling and do not decompose releasing the Ti or Zr ions. Furthermore, since the average number of valence electrons per atom, or valence electron concentration (VEC), for TiC and ZrC is VEC = 8 and TiN has VEC = 9 [17], respectively, but the n-ZrC additive exhibits the

weakest catalyzing effect (Figure 3) then their catalytic activity for mechanical dehydrogenation seems not to be related to their VEC number. It must, however, be pointed out that the n-TiN additive has the smallest average particle size of 20 nm and the largest SSA > 80 m^2/g. It also exhibits the fastest mechanical dehydrogenation rate in Figure 3. In turn, both n-TiC and n-ZrC have the average particle size on the order of 40 nm and n-TiC and n-ZrC has SSA = 50 m^2/g and > 70 m^2/g, respectively. However, despite that the SSA for n-ZrC is larger than that for n-TiC the mechanical dehydrogenation rate is higher for n-TiC than that for n-ZrC (Figure 3). Therefore, it seems that SSA or a particle size is not a major factor for the catalytic efficiency of n-TiC and n-ZrC. It was proposed [16] that the primary factor responsible for a strong catalytic effect of the nanometric n-TiN interstitial compound during mechanical dehydrogenation is its very small particle size on the order of 20 nm and the largest SSA > 80 m^2/g. The secondary factor, at a nearly equal particle size or SSA, seems to be a stronger catalytic effect for Ti than that for Zr in an interstitial compound.

In the cases discussed above a very efficient mechanical dehydrogenation phenomenon was induced by small amounts (5 wt.%) of non-hydride additives which were ball milled with the $LiAlH_4$ matrix. However, we also observed quite rapid mechanical dehydrogenation of the system in which $LiAlH_4$ was ball milled in a molar ratio 1:1 with a lithium amide ($LiNH_2$) hydride ($1LiAlH_4$ + $1LiNH_2$) [18]. Figure 4 shows that after 30 min (0.5 h) and 150–180 min (2.5 and 3 h) of ball milling the system releases as much as 4 and 5 wt.% H_2, respectively. We repeated the milling test in Figure 4 twice (1^{st} and 2^{nd} run) to confirm that the results are reproducible. As can be seen, the hydrogen desorption during ball milling is perfectly reproducible and the quantity of desorbed H_2 is nearly exactly the same for the 1^{st} and 2^{nd} run. For clarity, it is to be pointed out that the quantity of released H_2 rapidly decreased for the molar ratio ($3LiAlH_4$ + $LiNH_2$) and was not observed at all for the ratios $11.5LiAlH_4$ + $LiNH_2$) and ($30LiAlH_4$ + $LiNH_2$) [18]. The ($1LiAlH_4$ + $1LiNH_2$) hydride-hydride system has much higher initial rate of H_2 release (Figure 4) than the previously discussed systems of ($LiAlH_4$ + 5wt.% n-Fe)(Figure 1a) and ($LiAlH_4$ + 5 wt.% n-TiN/n-TiC/n-ZrC)(Figure 3).

In other words, the propensity of the lithium alanate-lithium amide system for mechanical dehydrogenation substantially decreases with increasing molar ratio of $LiAlH_4$ in the mixture. Since for the molar ratio ($1LiAlH_4$ + $1LiNH_2$) the mass content of $LiNH_2$ in the mixture equals 37.7 wt.% it means that this particular mass content of $LiNH_2$ in the mixture is a minimum required for efficient mechanical dehydrogenation. This behavior is quite puzzling. In order to obtain more insight into the phase changes occurring during ball milling as a function of milling time, X-ray diffraction (XRD) measurements were carried out on the composite samples extracted after pre-determined milling durations which are presented in Figure 5. As can be seen with increasing ball milling time to 0.5 (30 min), 1 and 3 h, the peaks become broadened and diffused as well as a pronounced uprising in the baselines and the formation of a broad "hump" in the range of $2\theta = 30–40°$ are observed which can be attributed to heavy nanostructuring or even the existence of increasing quantities of amorphous structure(s) [18]. The 100% intensity peaks for $LiAlH_4$, $LiNH_2$ and Li_3AlH_6 are visible after 0.5 and even after 1 h of milling although much weakened. There are also clear peaks which we assigned to Al. The presence of Li_3AlH_6 and Al in the microstructure of mechanically dehydrogenated ball milled samples clearly indicate that at least reaction described by Equation (1) must have occurred during ball milling. Furthermore, since the molar ratio ($1LiAlH_4$ + $1LiNH_2$) corresponds to a weight ratio of 62.3 wt.% $LiAlH_4$ and 37.7 wt.% $LiNH_2$, thus, at this weight ratio, fully completed reactions described by Equation (1) and (2) should provide approximately purity-corrected 3.2 and 1.6 wt.% H_2, respectively [18]. Since ~5 wt.% H_2 is released after 150 min ball milling (Figure 4) that means

that both reactions must have occurred during ball milling. As pointed out in [18] this is a peculiar observation because in a thermal DSC test, reaction described by Equation (1) is exothermic and that by Equation (2) is endothermic [3,4,19,20] which would suggest that both types of reactions, thermodynamically opposite, have been realized during high energy ball milling. However, since during ball milling the overall temperature increase in the milling vial is very small then the question arises whether the thermodynamic character of both reactions, which are now induced by mechanical energy, remains the same as that at elevated temperatures during DSC runs. Furthermore, it seems that the entire quantity of H_2 desorbed during ball milling of the 1:1 mixture (Figure 4) can be easily provided by reactions described by Equation (1) and (2). It was also argued in [18] that since the diffraction peaks of $LiNH_2$ in the 1:1 mixture persist throughout a long period of milling (Figure 5), it strongly indicates that $LiNH_2$ does not react/decompose but most likely becomes heavily nanostructured or even amorphized and in this capacity destabilizes $LiAlH_4$ during ball milling and enhances its decomposition according to reaction described by Equation (1) and (2) without involvement of any other reactions. However, as mentioned earlier, with decreasing molar content of $LiNH_2$ in the mixture, $LiNH_2$ somehow ceases to destabilize $LiAlH_4$ during ball milling. At the moment it is difficult to propose any detailed molecular mechanism by means of which the peculiar content of $LiNH_2$, equal to 37.7 wt.% for a 1:1 ratio, profoundly destabilizes $LiAlH_4$ during ball milling and, furthermore, the dependence of that mechanism on the molar ratio of the composite [18].

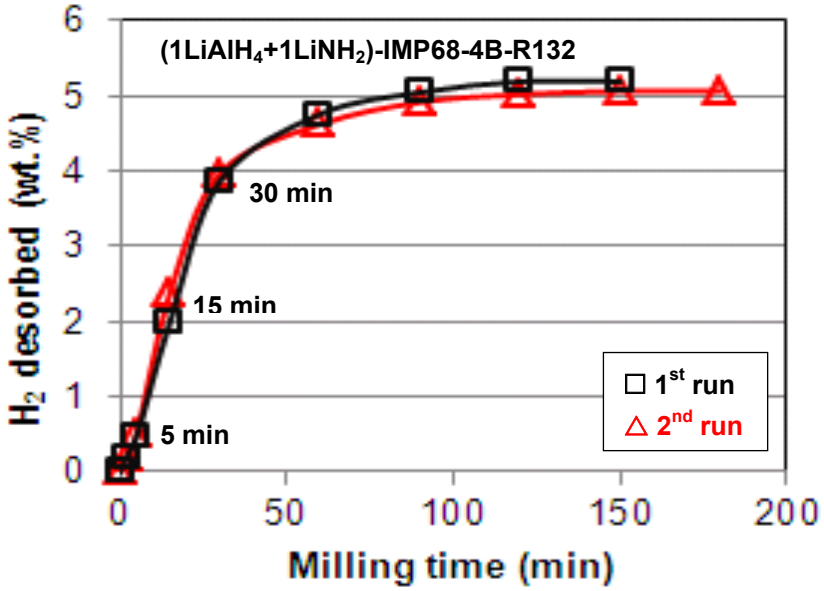

Figure 4. The quantity of H_2 desorbed by mechanical dehydrogenation during ball milling for the ($1LiAlH_4$ + $1LiNH_2$) molar mixture as a function of milling time [18].

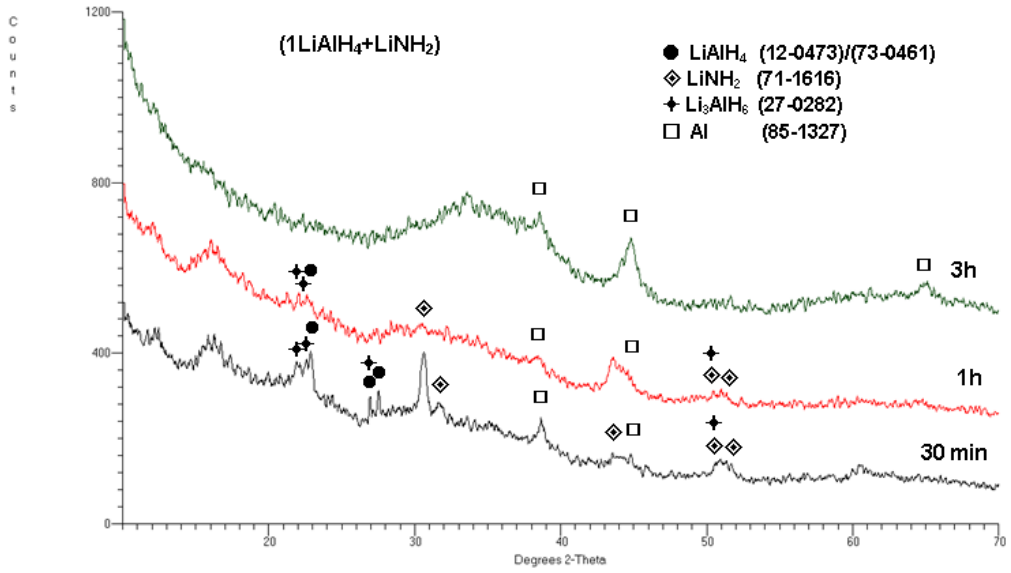

Figure 5. XRD patterns for ($1LiAlH_4 + 1LiNH_2$) after milling for 30 min, 1 h and 3 h. The ICDD file numbers for phase identification are shown in the legend [18].

Recently, we have investigated the effect of a manganese chloride ($MnCl_2$) additive on the hydrogen storage properties of $LiAlH_4$ for a wide range of molar ratios n in the ($nLiAlH_4 + MnCl_2$) system where n = 1, 3, 6, 8, 13, 30 and 63 (5 wt.% $MnCl_2$) [4,21]. This chloride is less volatile than those of Ti, V and Zr metals. Figure 6a shows that for the low molar ratios n = 1 to 13, the system releases substantial quantities of H_2 during ball milling with the maximum for n = 3. When the molar ratio n increases to 30 and 63 the quantity of released H_2 dramatically decreases. Figure 6b shows that for n = 3 ball milling up to barely 0.5 h (30 min) results in nearly 4 wt.% H_2 desorbed. At the first look this behavior is very similar to that for ($1LiAlH_4 + 1LiNH_2$) shown in Figure 4, in the sense, that the rate of mechanical dehydrogenation is rapid in the beginning of ball milling and subsequently saturates.

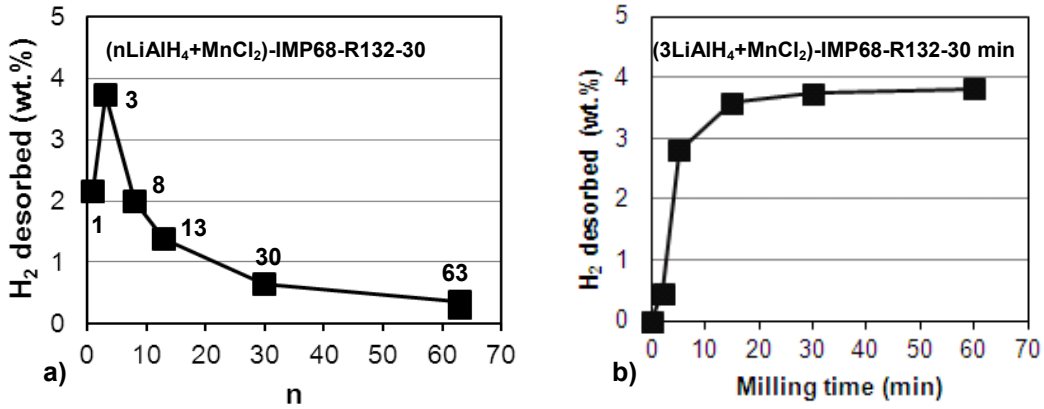

Figure 6. (a) The quantity of H_2 desorbed during ball milling of the ($nLiAlH_4 + MnCl_2$) mixture as a function of molar ratio n (shown by numbers) and (b) H_2 desorbed for n = 3 as a function of milling time [4,21].

Figure 7 shows the XRD patterns of the mixtures with the molar ratios n = 1 and 3 after ball milling for 0.5 h. The peak of copper (Cu) in both patterns arises from a support plate of the XRD sample holder used [4,21]. In the n = 1 mixture the principal diffraction peaks of the Li_2MnCl_4 compound are accompanied by minor peaks of LiCl, Al and a very broadened Mn peak which suggests that the Mn metal is heavily nanostructured. The Li_2MnCl_4 compound is an inverse cubic spinel that has been extensively studied for its ionic conductivity as a potential solid electrolyte for lithium-ion batteries [4,21]. Its formation during ball milling in the ($nLiAlH_4$ + $MnCl_2$) system has never been reported in the literature. The presence of Li_2MnCl_4, Al and Mn, combined with the fact that about 2 wt.% H_2 was desorbed within 0.5 h of ball milling (Figure 6a; n = 1), strongly suggests that following reaction must have occurred during milling for the molar ratio n = 1:

$$LiAlH_4 + MnCl_2 \rightarrow 0.5Li_2MnCl_4 + 0.5Mn + Al + 2H_2 \quad (3)$$

The total theoretical H_2 capacity of reaction described by Equation (3) is 2.46 wt.%. However, the presence of the LiCl peaks which form doublets with the Li_2MnCl_4 peaks in Figure 7 also suggests that another reaction was taking place during ball milling:

$$2LiAlH_4 + MnCl_2 \rightarrow 2LiCl + 2Al + Mn + 4H_2 \quad (4)$$

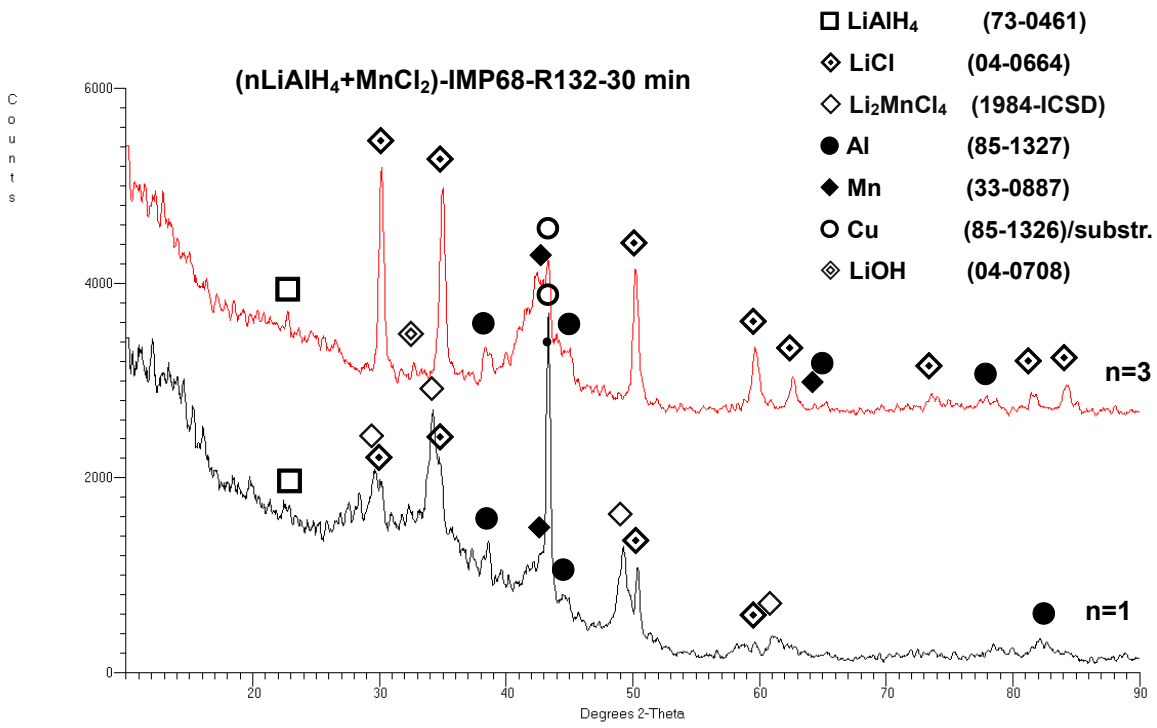

Figure 7. XRD patterns for the ($nLiAlH_4$ + $MnCl_2$) mixture where n = 1 and 3 ball milled for 30 min. ICDD file numbers are shown for peak identification [4,21].

Reaction described by Equation (4) has a theoretical H_2 capacity of 4 wt.%. It is not clear why this reaction occurred for the molar ratio n = 1. Normally, it should have occurred for the molar ratio n = 2. Perhaps, small powder volumes during milling were locally enriched to the n = 2 ratio. Figure

6a shows that about 2 wt.% H_2 was desorbed during milling for n = 1. That means that the principal reaction releasing H_2 was likely reaction described by Equation (3) with only a small fraction of H_2 released from reaction described by Equation (4). As shown in Figure 7 ball milling of the n = 3 system for 0.5 h produced principal phases LiCl, Mn, Al and a minority phase $LiAlH_4$. The observed weak peak of minor phase LiOH for n = 3 is an impurity commonly found in commercial $LiAlH_4$ [4,21]. Apparently, the presence of these phases suggests the following reaction:

$$3LiAlH_4 + MnCl_2 \rightarrow LiAlH_4 + 2LiCl + 2Al + Mn + 4H_2 \quad (5)$$

The theoretical capacity of this reaction is 3.4 wt.% H_2 and slightly less taking into account the purity of reactants (97% for $LiAlH_4$ and 99.99% for $MnCl_2$). The quantity of H_2 desorbed within 0.5 h of milling for n = 3 in Figure 6b is 3.7 wt.% which means that all H_2 from reaction described by Equation (5) was already desorbed during milling. The XRD patterns for the n = 6, 8, 13, 30 and 63 (5 wt.% $MnCl_2$) molar ratio always show the same phases LiCl, Mn, Al and $LiAlH_4$ after ball milling for 30 min [4,21], associated with H_2 release (Figure 13a). That means that for $n \geq 2$ reaction described by Equation (5) can be written in the following general form:

$$nLiAlH_4 + MnCl_2 \rightarrow (n-2)LiAlH_4 + 2LiCl + 2Al + Mn + 4H_2 \quad (6)$$

Apparently, in this case the H_2 desorption during ball milling occurs owing to simple chemical reaction in which $LiAlH_4$ is gradually consumed by reacting with $MnCl_2$ to produce LiCl, Al, Mn, possibly in a nanostructured form, and H_2. However, for n = 1 in addition to Al, Mn and LiCl an inverse cubic spinel phase, Li_2MnCl_4, is formed as a result of mechanical dehydrogenation according to Equation (3).

2.2. $LiNH_2$-MgH_2

The ($LiNH_2 + nMgH_2$) system is a hydride/hydride system that also exhibits the phenomenon of mechanical dehydrogenation during ball milling. Figure 8a shows the quantity of H_2 desorbed during ball milling for the ($LiNH_2 + nMgH_2$) system where n = 0.5 and 0.7 as a function of milling time. After 50 h of ball milling nearly 4 wt.% H_2 is desorbed as a result of mechanical dehydrogenation. In contrast to the previously discussed H_2 generating systems the rate of mechanical dehydrogenation for the ($LiNH_2 + nMgH_2$; n = 0.5 and 0.7) system is the lowest one of all investigated systems based on $LiAlH_4$. In the order of decreasing mechanical dehydrogenation rate, the systems can be ranked as follows: ($1LiAlH_4 + 1LiNH_2$) in Figure 4 (4 wt.% H_2 within 0.5 h), ($3LiAlH_4 + MnCl_2$) in Figure 6a (4 wt.% H_2 within 1 h), ($LiAlH_4$ + 5 wt.% n-Fe) in Figure 1a (3.6 wt.% H_2 within 5 h), ($LiAlH_4$ + 5 wt.% n-TiN/n-TiC) in Figure 3 (4 wt.% H_2 in 15 h and 6.6 wt.% H_2 within 18 h) and ($LiNH_2 + nMgH_2$; n = 0.5 and 0.7) in Figure 8a (4 wt.% H_2 within 50 h). Figure 8b shows the XRD patterns for the ($LiNH_2 + nMgH_2$) system (n = 0.5 and 0.7) ball milled for 50 h after release of about 4 wt.% H_2 as shown in Figure 2c. Both, the XRD in Figure 8b and FT-IR patterns (not shown here) indicate clearly that the following reactions occurred during milling [4,21,22]:

$$LiNH_2 + nMgH_2 \rightarrow 0.5Mg(NH_2)_2 + 1.0LiH + (n-0.5)MgH_2 \quad (7a)$$

$$0.5Mg(NH_2)_2 + 1.0LiH + [(n-0.5)MgH_2] \rightarrow 0.5Li_2Mg(NH)_2 + [(n-0.5)MgH_2] + 1.0H_2 \quad (7b)$$

The milling process depends on a number of parameters such as the geometry of milling device, milling mode, ball-to-powder weight ratio (R), dimensions of milling balls and milling time. This makes a direct comparison of milling results rather difficult. For our magneto-ball mill, the Uni-Ball-Mill 5, in which the milling processing discussed in this work was carried out, we derived by a semi-empirical method the universal milling parameter which is the milling energy input in kJ per unit mass (g) of powder, Q_{TR} (kJ/g), as described in detail in [22,23]. Therefore, Q_{TR} is a single, universal parameter by means of which any milling mode can be compared with another one after a specified milling time for a particular hydride composite system. Figure 9a shows the overall grain size changes for various milling modes and R ratios as a function of injected energy input (Q_{TR}). It is clearly seen that the $LiNH_2$ grain size decreases rapidly with increasing Q_{TR} reaching the size range 10–50 nm at the Q_{TR} = 150–200 kJ/g and subsequently more or less saturates. Figure 9b shows the variations of grain size for $LiNH_2$ and MgH_2 constituents for a fixed molar ratio n = 0.7 ($LiNH_2$ + 0.7MgH_2) and a constant ball-to-powder mass ratio, R = 40, as a function of injected energy Q_{TR40}. The crystallite (grain) size decreases rapidly with increasing Q_{TR} up to approximately 150–200 kJ/g and subsequently more or less saturates at the value of 10–20 nm. Also, Figure 9a shows that a relatively low Q_{TR} is sufficient to reach the grain size of 100 nm for $LiNH_2$ which is considered a threshold value for attaining a nanocrystalline structure [22]. The lattice strain has been found to be minimal (0.12–0.49%) [22].

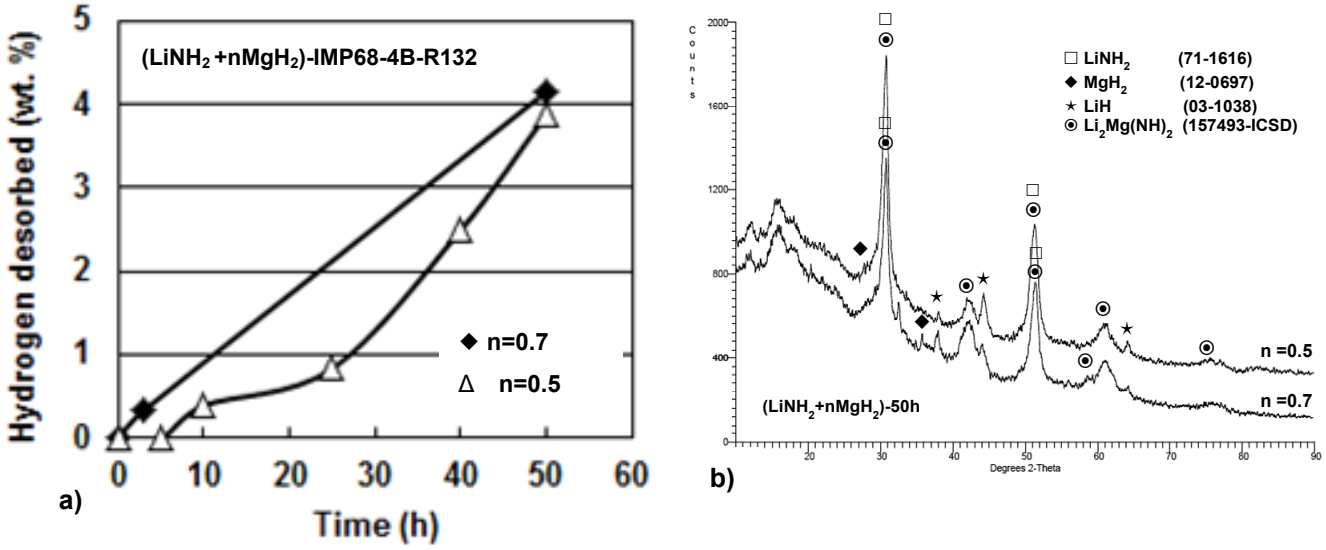

Figure 8. (a) (c) The quantity of H_2 desorbed during ball milling for the ($LiNH_2$ + $nMgH_2$) system where n = 0.5 and 0.7. (b) XRD patterns for the ($LiNH_2$ + $nMgH_2$) system where n = 0.5 and 0.7, ball milled for 50h under a high energy mode IMP68-4B-R132 (the ICDD file numbers for phase identification are shown) [4,21,22].

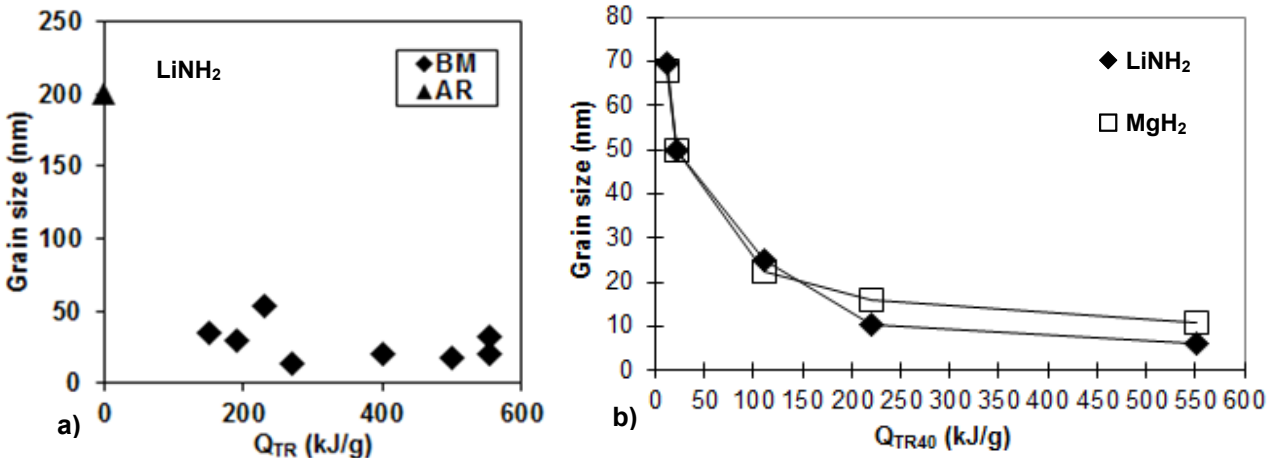

Figure 9. Estimated grain (crystallite) size as a function of milling energy input for (a) $LiNH_2$ in all ($LiNH_2$ + nMgH_2; n = 0.5, 0.7, 0.9, 1.0 and 2.0) nanocomposites and (b) $LiNH_2$ and MgH_2 for the ($LiNH_2$ + 0.7MgH_2) mixture milled under the IMP68-4B-R40 mode. AR-as received, BM-ball milled [22].

2.3. Complex borohydride synthesized by mechano-chemical activation synthesis (MCAS)

Some of those new complex borohydride systems are derivatives of lithium borohydride (tetrahydroborate), $LiBH_4$, which is a commercially available, high capacity complex metal hydride having the highest theoretical gravimetric H_2 capacity (18.5 wt.%) and good volumetric capacity (122.5 kgH_2/m^3) [24]. It is well established [24,25] that at around 100–118 °C, $LiBH_4$ undergoes a polymorphic transformation from the orthorhombic *Pnma* crystal structure to the hexagonal *P63mc* crystal structure which is followed by melting around 280 °C and subsequent dehydrogenation reaction in the following form:

$$LiBH_4\,(l) \rightarrow LiH\,(s) + B\,(s) + 3/2H_2\,(g) \quad (8)$$

where l-liquid, s-solid and g-gas. The theoretical maximum quantity of H_2 desorbed in Equation (8) is 13.9 wt.%. Since LiH is very stable and can only be decomposed at temperatures in excess of 700 °C [25] the rest of the total H_2 capacity from $LiBH_4$ is not easily accessible.

To complicate the case even more, the enthalpy and entropy changes (ΔH and ΔS) for reaction (1) are reported as ΔH = 68.9 $kJ/molH_2$ and ΔS = 100.2 $J/KmolH_2$ [26] and ΔH = 74 $kJ/molH_2$ and ΔS = 115 $J/KmolH_2$ [27] which indicate that reaction described by Equation (8) is endothermic. According to the Van't Hoff equation [3–5]:

$$\ln (p/p_0) = -\Delta H/RT + \Delta S/R \quad (9)$$

where p is the pressure (atm or bar), p_0 is the atmospheric pressure (1 atm or 1 bar), ΔH and ΔS are the enthalpy and entropy changes in $kJ/molH_2$ and $J/KmolH_2$, respectively, R is the gas constant (8.314472 J/molK) and T is the absolute temperature (K). Therefore, the decomposition temperature of $LiBH_4$, according to reaction (8) at 1 bar H_2 pressure will be in excess of 370 °C. That means that even the quantity of 13.9 wt.% H_2 from reaction described by Equation (8) is practically unavailable for fueling

a PEM FC stack which generates a waste heat temperature 70–80°C (max. 100°C) as mentioned earlier.

However, $LiBH_4$ can be destabilized in solid state by transforming it into other complex metal hydrides, more suitable for H_2 generation. In these cases a mechano chemical activation synthesis (MCAS) by ball milling was used to induce chemical reactions between $LiBH_4$ and an appropriate metal chloride (MCl_n; M-metal) which resulted in the formation of new metal borohydrides, always mixed with LiCl, the latter being a by-product of MCAS reaction [28,29].

In due course of our experimental work on fast hydrogen generating hydrides (or their mixtures) mentioned above, we recently noticed a high proclivity of the ($2LiBH_4 + FeCl_2$) hydride/chloride system to rapidly generate H_2 during ball milling at the ambient temperature, without any external heating [30]. Figure 10 shows the effects of increasing milling energy input, Q_{TR}, on the mechanical dehydrogenation of samples. A minimal amount of 0.33 wt.% H_2 is released due to mechanical dehydrogenation after injection of 2.43 kJ/g milling energy (Figure 10a) which increases to 0.87 wt.% H_2 after injecting nearly 3-fold quantity of milling energy (6.07 kJ/g)(Figure 10b). The quantity of H_2 due to mechanical dehydrogenation rapidly increases to 2.80 (Figure 10c), 3.50 (Figure 10d) and 4.02 wt.% (Figure 10e) after injecting 12.14, 18.2 and 36.4 kJ/g of milling energy input, respectively. Since the total theoretical H_2 capacity of the ($2LiBH_4 + FeCl_2$) mixture is 4.73 wt.%, injecting barely 36.4 kJ/g of milling energy input (0.5 h (30 min) ball milling under the mode shown) leads, at the ambient temperature, to mechanical dehydrogenation of about 85% of the theoretical H_2 capacity (Figure 10e), or even slightly higher if one takes into account the purity corrected total capacity. It is also clear that if the H_2 quantity released by mechanical dehydrogenation is approximately below 4 wt.% (Figure 10a–d), subsequent thermal dehydrogenation of the ball milled samples releases slightly more H_2 although with a dehydrogenation rate lower than that for mechanical dehydrogenation. Apparently, the mechanical dehydrogenation rate at the ambient temperature is found to be much higher than the thermal dehydrogenation rate at the 100 and 250 °C range (not shown here). To achieve that remarkable H_2 desorption rate the required milling energy input is very small, 36.4 kJ/g which is another beneficial aspect of the investigated solid state chemical system. This is a very beneficial behavior, indeed, for a rapid H_2 generator, clearly indicating that elevated temperature is not really needed for desorbing large quantities of H_2 but just a very small quantity of mechanical energy is sufficient.

Figure 11 shows the XRD pattern as a function of milling energy input (milling time) for samples whose mechanical dehydrogenation curves are shown in Figure 10. It is clearly seen that the peaks of $LiBH_4$ disappear just after the milling energy input reaches 2.43 kJ/g while the peaks of $FeCl_2$ disappear after about 12.14 kJ/g of milling energy input. The peaks of LiCl become visible after the injection of 6.07 kJ/g milling energy. Such a rapid disappearance of the $LiBH_4$ peaks without yet visible formation of LiCl suggests that $LiBH_4$ becomes highly disordered by ball milling. The presence of LiCl after ball milling, which is not accompanied by any other diffraction peaks, strongly indicates that metathesis (double substitution) reaction occurred between $LiBH_4$ and $FeCl_2$ forming LiCl and unknown hydride that does not have a regular crystallographic structure that would allow X-ray diffraction. Furthermore, this hydride subsequently decomposes during continuous ball milling releasing hydrogen. This observation is in a good agreement with Nakamori et al. [28,29] who reported formation of disordered hydrides $M(BH_4)_n$ (M-metal) that did not produce any diffraction patterns when they used metal chlorides, MCl_n where M = Cr, Mg, Mn, Zr, Ti, V, Zn, Ca, Sc, Al for mechano-chemical activation synthesis. According to Nakamori et al. [28,29] those

disordered complex metal hydrides do not exhibit a long-range order of the M^{n+} and $(BH_4)^{n-}$ units but they do have a short-range order. Taking into consideration our XRD results in Figure 11 and a couple papers on either wet reaction of $LiBH_4$ and $FeCl_2$ in diethyl ether [31] or mechano-chemical synthesis [32], we hypothesize that a rapid rate of mechanical dehydrogenation is the result of the formation of a metastable, disordered iron borohydride, d-$Fe(BH_4)_2$, which rapidly decomposes during continuous ball milling (BM) releasing H_2 according to following reaction:

$$LiBH_4 + 0.5FeCl_2 \rightarrow (\mathbf{BM}) \rightarrow 0.5\text{d-}Fe(BH_4)_2 + LiCl \rightarrow (\mathbf{BM}) \rightarrow 0.5\text{a-Fe} + \text{a-B} + 2H_2 + [LiCl] \quad (10)$$

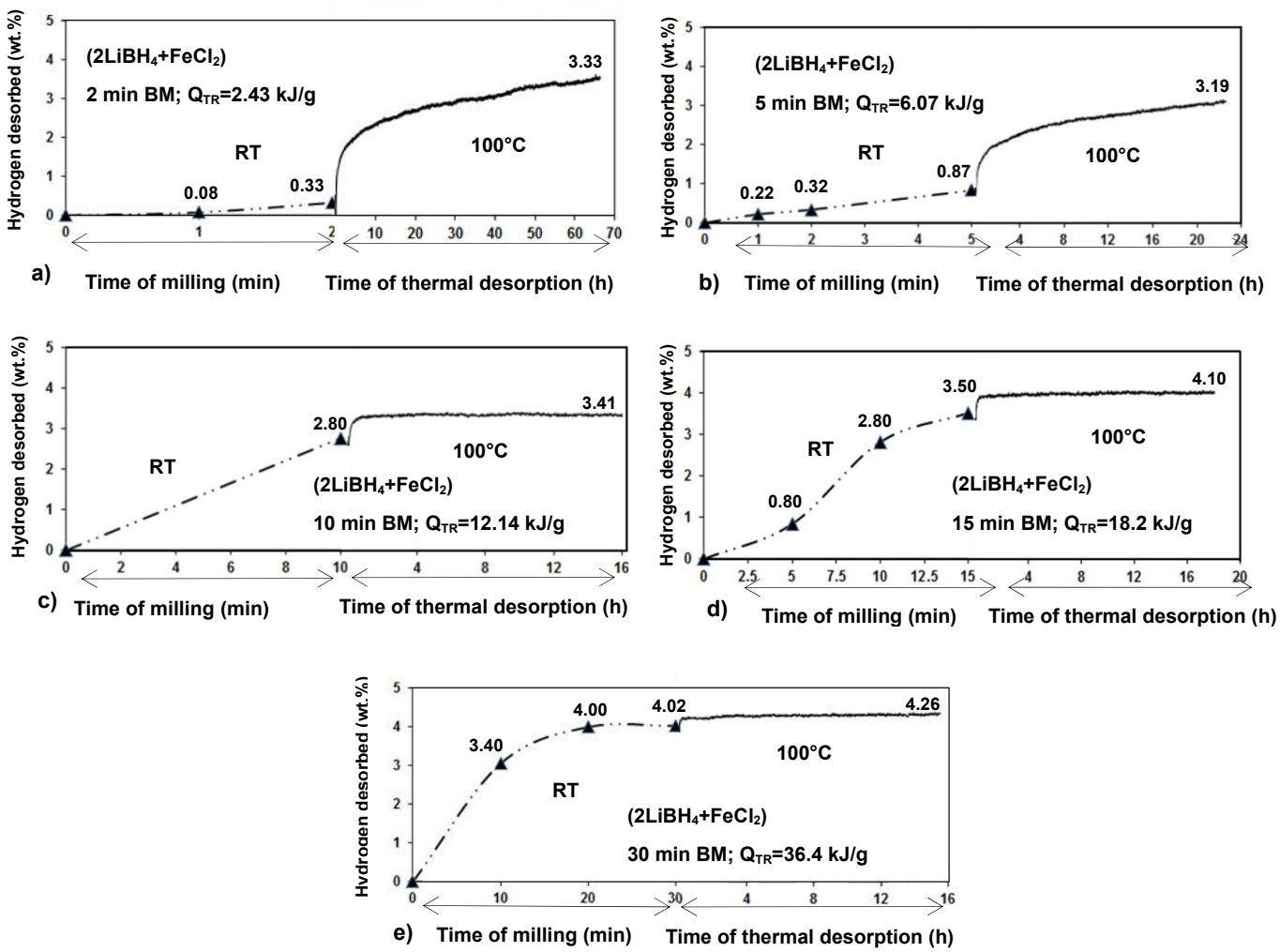

Figure 10. Hydrogen desorption curves for ($2LiBH_4$+$FeCl_2$) after (a) 2 min BM (Q_{TR} = 2.43 kJ/g), (b) 5 min BM (Q_{TR} = 6.07 kJ/g), (c) 10 min BM (Q_{TR} = 12.14 kJ/g), (d) 15 min BM (Q_{TR} = 18.20 kJ/g) and (e) 30 min BM (Q_{TR} = 36.40 kJ/g). All milled powders were subsequently dehydrogenated at 100°C and the pertinent curves are shown [30].

In the decomposition part of above reaction, a salt, LiCl, which is a dead-weight, coexisting with amorphous iron (a-Fe) and amorphous boron (a-B) are being formed. The brackets for [LiCl] mean that LiCl does not take part in decomposition reaction. It is to be pointed out that all ball milled

samples exhibit ferromagnetic behavior being strongly attracted to a magnet. This is good supporting evidence of the presence of α-Fe in the microstructure. Also, Fourier transform-infrared (FT-IR) spectra show the presence of a new borohydride, most likely, d-Fe$(BH_4)_2$ after ball milling [30].

So far, the ($2LiBH_4$ + $FeCl_2$) system exhibits the highest rate of mechanical dehydrogenation releasing 4.02 wt.% H_2 after injecting a very small milling energy input of barely 36.4 kJ/g (0.5 h milling). For comparison, the earlier discussed ($1LiAlH_4$ + $LiNH_2$) hydride/hydride (Figure 4) and ($3LiAlH_4$ + $MnCl_2$) hydride/halide (Figure 6) systems were capable of mechanical dehydrogenation of 3.7 wt.% H_2 after injecting the same 36.4 kJ/g quantity of milling energy input. The other hydride systems, already discussed, exhibit a much lower mechanical dehydrogenation rate. The quantity of 4 wt.% H_2 released from the ($LiAlH_4$ + 5 wt.% n-Fe), ($LiAlH_4$ + 5 wt.% n-TiN) and ($LiNH_2$ + (0.5 and 0.7) MgH_2) hydride systems, required a milling energy input of 364 (Figure 1a), 1090 (Figure 3) and 3600 kJ/g (Figure 8a), respectively, converting the milling time required for the release of 4 wt.% H_2 into the energy input as described in Sec. 2.2.

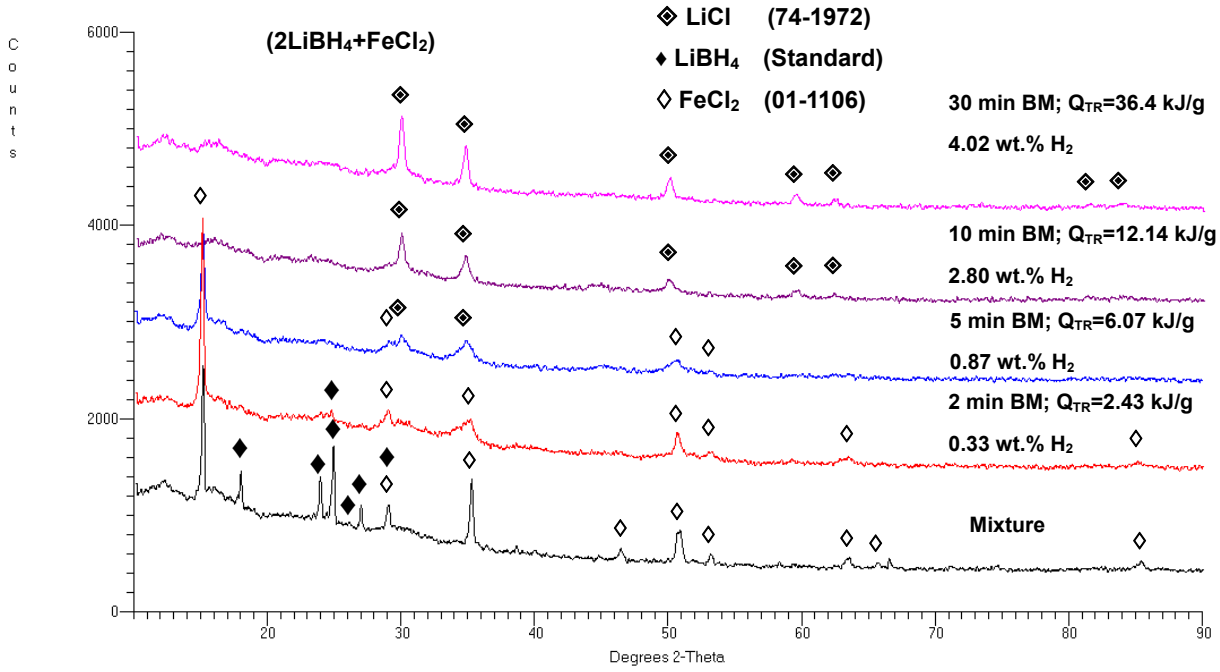

Figure 11. XRD patterns of the ($2LiBH_4$ + $FeCl_2$) mixture ball milled (BM) with increasing milling energy input Q_{TR} (milling time). The quantity of H_2 released (wt.%) through mechanical dehydrogenation is indicated. ICDD file numbers are shown for peak identification [30].

3. Hydrogen Generating Systems at Low Elevated Temperatures (100 °C)

A $LiAlH_4$ hydride with catalytic metal and interstitial compounds additives, which was discussed in the preceding sections, in its capacity as a rapid H_2 generator through mechanical dehydrogenation during ball milling, is also capable of desorbing H_2 at temperatures that do not exceed 100 °C. In this case the $LiAlH_4$ mixture with additives must be ball milled under conditions under which no mechanical dehydrogenation occurs. Figure 12 shows volumetric dehydrogenation

curves at 100 °C for $LiAlH_4$ with added 5 wt.% n-Ni [19] and n-Fe [14] (Figure 11a), and 5 wt.% n-TiC/n-TiN/n-ZrC (Figure 11b) [16] which were ball milled with the milling energy input Q_{TR} = 18.2 kJ/g (IMP68-4B-R132-15 min) [19], Q_{TR} = 18.4 kJ/g (IMP68-2B-R132-15 min)[14] and Q_{TR} = 18.2 kJ/g (IMP68-4B-R132-15 min) [16], respectively. This small quantity of injected milling energy input did not induce mechanical dehydrogenation. As can be seen, the ball milled nanocomposite ($LiAlH_4$ + 5 wt.% n-Ni/n-Fe) is capable of desorbing close to 7 wt.% H_2 within ~25 h duration while its ball milled counterpart containing 5 wt.% n-TiN/n-TiC/n-ZrC desorbs the same quantity of H_2 within a slightly shorter duration of about 16 h at 100 °C. The desorption curves clearly indicate that H_2 desorption occurs in two stages where the rapid desorption Stage I corresponds to reaction described by Equation (1) and a slow Stage II corresponds to reaction described by Equation (2) [14,16,19]. Furthermore, it has been found [16] that the interstitial compound additives do not substantially affect the apparent activation energy of Stage I dehydrogenation but are able to strongly reduce the apparent activation energy of Stage II dehydrogenation. Accordingly, for thermal dehydrogenation in Stage I the average apparent activation energy, E_A, for the interstitial additives is within the range of 87–96 kJ/mol whereas, for comparison, the metallic additives of n-Fe and n-Ni show drastically smaller apparent activation energy on the order of 55–58 kJ/ mol, most likely, due to the $LiAlH_4$ lattice destabilization. The average apparent activation energy for thermal dehydrogenation in Stage II is in the range of 63–80 kJ/mol in the order of E_A (n-ZrC) < E_A (n-TiN = n-TiC) and is lower than that for the nanometric metal additives n-Ni and n-Fe [16]. We have not observed successful rehydrogenation for $LiAlH_4$ containing 5 wt.% of nanometric n-Ni/n-Fe or n-ZrC/n-TiN/n-TiC additives under the pressure up to 100 bar H_2 and temperatures within the range 55–250 °C for several hours which clearly indicates that $LiAlH_4$ with catalytic additives is irreversible. However, it has been found [33,34] that $LiAlH_4$ which was initially ball milled with TiCl and subsequently dehydrogenated to a mixture of (LiH + Al) according to Equation (2), could be partially rehydrogenated back to $LiAlH_4$ at room temperature in low-boiling dimethyl ether under 100 bar H_2 pressure.

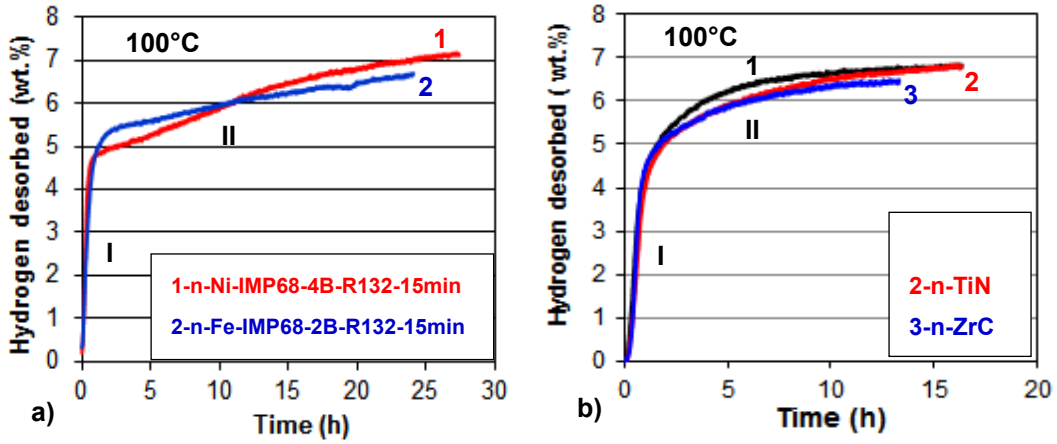

Figure12. Volumetric dehydrogenation curves at 100°C for ball milled $LiAlH_4$ with added (a) 5 wt.% n-Ni [19] and n-Fe [14], and (b) 5 wt.% n-TiC, n-TiN and n-ZrC [16].

Another hydride recently synthesized in our laboratory is a manganese borohydride, $Mn(BH_4)_2$ [35,36,37]. Its theoretical H_2 capacity is 9.5 wt.%. This borohydride has been successfully synthesized by the mechano-chemical activation synthesis (MCAS) of the ($MnCl_2$ + $nLiBH_4$) mixture, where n a number of moles $LiBH_4$. Measurements of the particle size showed that the average particle size of 7.5 ± 2.6 μm is the smallest one after milling for 2 h with Q_{TR} = 145.6 kJ/g. After milling for 5 h with Q_{TR} = 364 kJ/g the average particle size increases to 16.1 ± 6.3 μm due to agglomeration of particulate [37]. However, it must be kept in mind that the individual powder particles forming an agglomerate could be much smaller than the average value. Figure 13 shows the XRD pattern for the ball milled n = 2 and 3 nanocomposites after MCAS with the milling energy input Q_{TR} = 145.6 kJ/g (a milling mode IMP68-4B-R132-2h). Only the diffraction peaks of LiCl and $Mn(BH_4)_2$ are clearly seen. The identification of $Mn(BH_4)_2$ was based on the data reported in [38–40] which show that it has a trigonal/hexagonal lattice structure (the space group $P3_112$) with the lattice parameters a = 10.435(1)Å and c = 10.835(2)Å. The pattern for the n = 3 nanocomposite is nearly identical to the n = 2 nanocomposite with the exception that a remnant very weak and broad $LiBH_4$ peak is barely visible. Nearly identical XRD patterns were observed after milling with a much lower energy input, Q_{TR} = 36.4 kJ/g (0.5 h). Based on the XRD and FT-IR analysis [37] it is clear that the synthesis of $Mn(BH_4)_2$ occurs according to "metathesis" reaction during MCAS described by:

$$MnCl_2 + nLiBH_4 \rightarrow Mn(BH_4)_2 + 2LiCl + (n-2)LiBH_4 \quad (11)$$

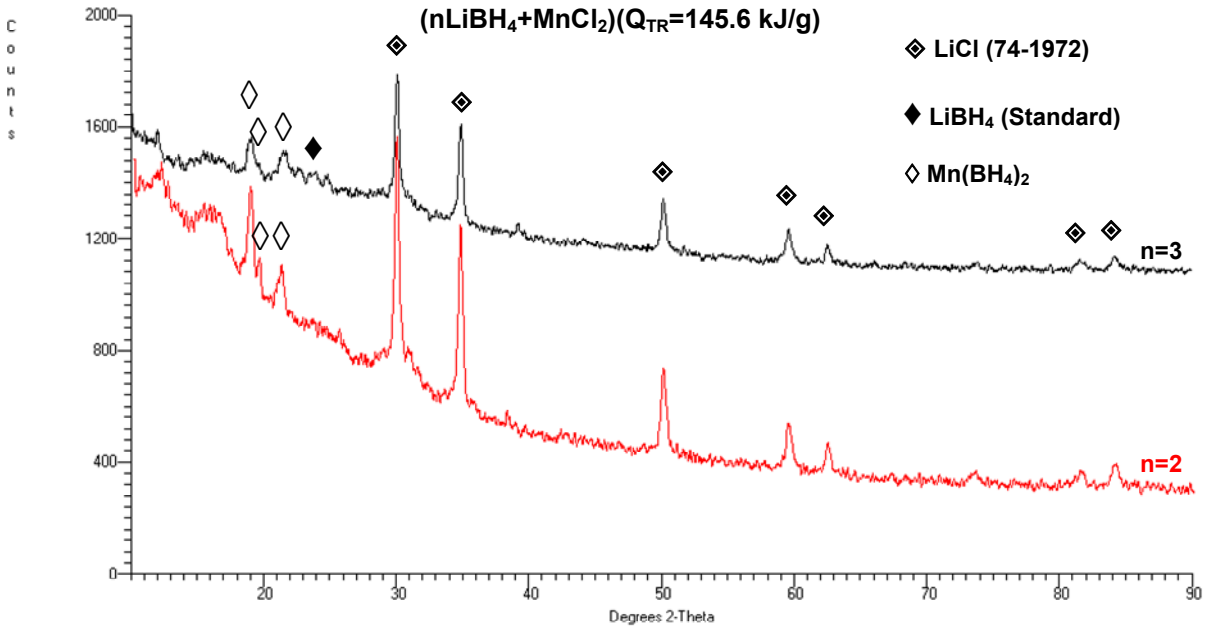

Figure 13. XRD patterns after ball milling (BM) with the energy input, Q_{TR} = 145.6 kJ/g, for the n = 2 and 3 mixtures. ICDD file number shown for LiCl [37].

As a result of reaction in Equation (11), simultaneously with $Mn(BH_4)_2$ a by-product LiCl is also formed which is just a "dead-weight" for the system reducing the overall H_2 capacity. It is quite remarkable that "metathesis" reaction in Equation (11) is able to occur at a small input of milling energy Q_{TR} = 36.4 kJ/g. It suggests that a thermodynamic barrier for "metathesis" reaction in a

$LiBH_4/MnCl_2$ system is very low. The peaks of $Mn(BH_4)_2$ and LiCl are broadened that confirm that the synthesized hydride is heavily nanostructured. The calculations of crystallite (grain) size showed that the synthesized $Mn(BH_4)_2$ hydride is nanocrystalline exhibiting a crystallite (grain) size within the range from ~21 to ~14 nm which slightly decreases with increasing milling energy input, Q_{TR}. The crystallite (grain) size of LiCl is very close to 30 nm regardless of the milling energy input, Q_{TR} [37].

Figure 14 shows the desorption curves at 100 °C for small and medium milling energy inputs during MCAS synthesis. The maximum H_2 desorption quantity is very similar for both milling energy inputs and does not exceed ~4.5 wt.%. The maximum theoretical H_2 capacity for the n = 2 mixture ($2LiBH_4 + MnCl_2$) is 4.76 wt.% (Table 1 in Reference [36]). Since the maximum H_2 quantity desorbed in Figure 14 is no larger than the maximum theoretical H_2 capacity then it is clear that no measurable diborane gas (B_2H_6) was desorbed as also evidenced by gas mass spectroscopy reported in [36]. XRD patterns after desorption at 100°C did not show peaks of $Mn(BH_4)_2$ [36] which means that the synthesized hydride completely decomposed during dehydrogenation according to reaction Equation (12):

$$Mn(BH_4)_2 \rightarrow Mn + 2B + 4H_2 \quad (12)$$

No XRD peaks of Mn and B, as would be required by reaction Equation (12), were observed in [36] which strongly confirms that both elements are amorphous after dehydrogenation.

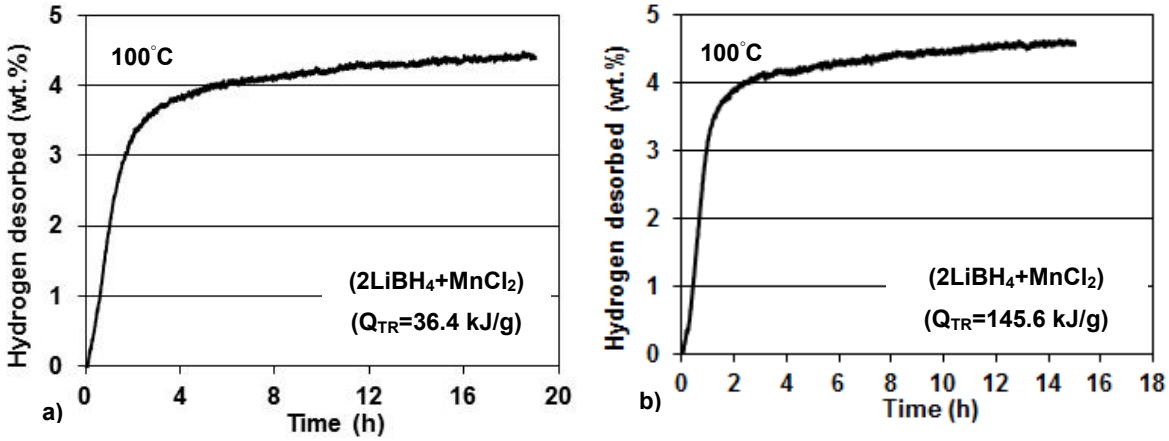

Figure 14. Dehydrogenation curves at 100 °C for the n = 2 nanocomposite ball milled with the energy input Q_{TR} (a) 36.4 and (b) 145.6 kJ/g [37].

The values of the apparent activation energy for dehydrogenation reported in [37] were very low. The apparent activation energy for the n = 3 nanocomposite decreased monotonically from ~70 to ~59 kJ/mol with increasing milling energy input whereas the apparent activation energy for the n = 2 nanocomposite decreased from about 65 kJ/mol for Q_{TR} = 36.4 kJ/g to about 53 kJ/mol for Q_{TR} = 145.6 kJ/g and then again increased to ~59 kJ/mol for the Q_{TR} = 364 kJ/g. These changes closely followed the variations in the average powder particle size obtained with the varying milling energy input suggesting that for the n = 2 ratio the apparent activation energy seems to somehow depend on the particle size rather than the crystallite (grain) size of $Mn(BH_4)_2$. Since the LiCl by product is

useless and just reduces the maximum capacity of H_2 available from the $Mn(BH_4)_2$-LiCl system, it must be removed by chemical methods (Soxhlet extraction) [37].

4. Discussion

In the present comprehensive review two important groups of complex hydride systems for hydrogen generation are being reviewed. In the first group, the hydride systems that are capable of generating H_2 through mechanical dehydrogenation phenomenon at the ambient temperature are discussed. There are few diverse systems in this group such as lithium alanate ($LiAlH_4$) with such additives as nanoiron (n-Fe), lithium amide ($LiNH_2$) (a hydride/hydride system), and manganese chloride $MnCl_2$ (a hydride/halide system), as well as another hydride/hydride system consisting of lithium amide ($LiNH_2$) and magnesium hydride (MgH_2), and finally, a hydride/halide $LiBH_4$-$FeCl_2$ system. These hydride systems are capable of releasing from ~4 to ~7 wt.% H_2 at the ambient temperature during relatively short duration ball milling. The second group encompasses systems that generate H_2 at only slightly elevated temperatures (up to 100 °C). In this group, lithium alanate ($LiAlH_4$) ball milled with the nanometric n-Fe and n-TiN/n-TiC/n-ZrC additives is a prominent system that can relatively fast generate up to 7 wt. % H_2 at 100°C. The other hydride is manganese borohydride ($Mn(BH_4)_2$) synthesized by mechano-chemical activation synthesis (MCAS). In a ball milled nanocomposite co-existing with LiCl, $Mn(BH_4)_2$ can desorb ~4.5 wt.% H_2 at 100 °C within a reasonable dehydrogenation time.

It is interesting for the readership to discuss shortly some practical application aspects of the hydrides reviewed in the preceding sections. It must be clearly reiterated that the hydride systems for hydrogen generation are not typical, reversible on board, hydrogen "storage" systems in the classical meaning of this word. In contrast to typical "on-board" storage systems, the H_2 generating systems, after being exhausted and converted into elemental or other chemical species, would not require reversibility "on-board" but could be chemically regenerated or converted to useful chemical compounds "off-board", i.e. in a chemical plant.

For example, it may be envisaged that the rapid mechanical dehydrogenation phenomenon occurring at the ambient temperature, discussed earlier in the present review for some hydride/nano-metal/nano-interstitial compound ($LiAlH_4$ + 5 wt.% n-Fe/n-TiN/n-TiC/n-ZrC), hydride/hydride ($1LiAlH_4$ + $1LiNH_2$) and hydride/halide ($3LiAlH_4$ + $MnCl_2$ and $2LiBH_4$-$FeCl_2$) systems, could be applied in practical engineering terms for generating large quantities of hydrogen on demand for auxiliary power generation systems coupled with PEM fuel cells and batteries. Further possible practical applications for the rapid hydrogen generators are low power remote fuel cells or portable gas analyzers [41,42], fuel cell off-road vehicles and cordless lawn mowers running with a fuel cell instead of hydrogen combustion engine [43]. The rapid H_2 generators can also be used in a number of chemical processes where a continuously reducing atmosphere is needed for a completion of the chemical process [4]. They could also have an application in a military sector for supplying hydrogen to micro fuel cells in portable devices needed for soldiers on a mission in remote areas [4].

Furthermore, a surprisingly very low mechanical energy input required to generate H_2 from several such systems like ($1LiAlH_4$ + $1LiNH_2$) and ($2LiBH_4$ + $FeCl_2$), without the necessity for applying elevated temperatures, renders the rapid mechanical dehydrogenation phenomenon useful for powering various fuel cell-run devices mentioned above in such a way that the mechanical

energy for H_2 release could even be provided by human power similarly, for instance, to pedaling a stationary bicycle.

Other hydride/hydride or hydride/halide systems with even more rapid mechanical dehydrogenation rate and higher released H_2 capacity, which could practically serve as "rapid mechanical hydrogen generators" should be sought. Several similar high H_2 capacity systems are now under investigation in our laboratory and will be reported in further publications.

Acknowledgements

This research was financially supported by a Natural Sciences and Engineering Research Council (NSERC) of Canada Discovery Grant which is gratefully acknowledged.

Conflict of Interest

All authors declare no conflicts of interest in this paper.

References

1. Scott DS (2007) Smelling land-the hydrogen defense against climate catastrophe, Westmount, QC: Canadian Hydrogen Association.
2. Bockris JOM (2007) Will lack of energy lead to the demise of high-technology countries in this century? *Int J Hydrogen Energ* 32: 153–158.
3. Varin RA, T. Czujko T, Wronski ZS (2009) Nanomaterials for solid state hydrogen storage. New York, Springer Science, 2009. Business Media.
4. Varin RA, Wronski ZS (2013) Progress in hydrogen storage in complex hydrides. In: Gandia LM, Arzamendi G, Diéguez PM, *Renewable Hydrogen Technologies. Production, Purification, Storage, Applications and Safety*, Elsevier: Ch. 13; 293–332.
5. Yang J, Sudik A, Wolverton C, et al. (2010) High capacity hydrogen storage materials: attributes for automotive applications and techniques for materials discovery. *Chem Soc Rev* 39: 656–675.
6. Rude LH, Nielsen TK, Ravnsbæk DB, et al. (2011) Tailoring properties of borohydrides for hydrogen storage: A review. *Phys Status Solidi A* 208: 1754–1773.
7. Department of Energy US. Available from: http://energy.gov/sites/prod/files/2014/03/f12/targets_onboard_hydro_storage.pdf.
8. Li H-W, Yan Y, Orimo S-I, et al. (2011) Recent progress in metal borohydrides for hydrogen storage. *Energies* 4: 185–214.
9. Toyota Hydrogen Fuel Cell Vehicles to be Available in 2016. Available from: http://www.hngn.com/articles/33584/20140612/toyota-hydrogen-fuel-cell-vehicles-to-be-available-in-2016.htm.
10. Hyundai first to offer hydrogen fuel cell vehicles to Canadian public. Available from: http://www.newswire.ca/en/story/1453489/hyundai-first-to-offer-hydrogen-fuel-cell-vehicles-to-canadian-public.
11. Calka A, Radlinski AP (1991) Universal high performance ball-milling device and its application for mechanical alloying. *Mater Sci Eng* A 134: 1350–1353.
12. Patents: WO9104810, US5383615, CA2066740, EP0494899, AU643949.

13. Calka A, Varin RA (2001) Application of Controlled Ball Milling in Materials Processing. In: Srivatsan TS, Varin RA, Khor M, *Int. Symp. on Processing and Fabrication of Advanced Materials IX (PFAM IX)*. ASM International: Materials Park, OH, 263–287.
14. Varin RA, Parviz R (2012) The effects of the micrometric and nanometric iron (Fe) additives on the mechanical and thermal dehydrogenation of lithium alanate ($LiAlH_4$), its self-discharge at low temperatures and rehydrogenation. *Int J Hydrogen Energ* 37: 9088–9102.
15. WebElements Periodic Table: the periodic table on the web. Available from: http://webelements.com.
16. Varin RA, Parviz R (2014) The effects of the nanometric interstitial compounds TiC, ZrC and TiN on the mechanical and thermal dehydrogenation and rehydrogenation of the nanocomposite lithium alanate ($LiAlH_4$) hydride. *Int J Hydrogen Energ* 39: 2575–2586.
17. Girgis K (1983) Structure of intermetallic compounds, In: *Physical Metallurgy*; third, revised and enlarged edition; Cahn RW and Haasen P, Elsevier Science Publishers, BV, Part I, Ch.5, 220–269.
18. Varin RA, Zbroniec L (2012) Mechanical and thermal dehydrogenation of lithium alanate ($LiAlH_4$) and lithium amide ($LiNH_2$) hydride composites. *Crystals* 2: 159–175.
19. Varin RA, Zbroniec L (2010) The effects of nanometric nickel (Ni) catalyst on the dehydrogenation and rehydrogenation behavior of ball milled lithium alanate ($LiAlH_4$). *J Alloy Compd* 506: 928-939.
20. Varin RA, Zbroniec L, Czujko T, Wronski ZS (2011) The effects of nanonickel additive on the decomposition of complex metal hydride $LiAlH_4$ (lithium alanate). *Int J Hydrogen Energ* 36*:* 1167–1176.
21. Varin RA, Parviz R, Zbroniec L, Wronski ZS (2012) Fundamental aspects of mechanical dehydrogenation of Li-based complex hydride nanocomposites and their self-discharge at low temperatures. *Energy Procedia* 29: 644–653.
22. Parviz R, Varin RA (2013) Combined effects of molar ratio and ball milling energy on the phase transformations and mechanical dehydrogenation in the lithium amide-magnesium hydride ($LiNH_2 + nMgH_2$) (n = 0.5–2.0) nanocomposites. *Int J Hydrogen Energy* 38: 8313–8327.
23. Varin RA, Parviz R, Polanski M, et al. (2014) The effect of milling energy input and molar ratio on the dehydrogenation and thermal conductivity of the ($LiNH_2 + nMgH_2$) (n = 0.5, 0.7, 0.9, 1.0, 1.5 and 2.0) nanocomposites. *Int J Hydrogen Energ* 39: 10585–10599.
24. Orimo SI, Nakamori Y, Eliseo JR, et al. (2007) Complex hydrides for hydrogen storage. *Chem Rev* 107: 4111–4132.
25. Züttel A, Rentsch S, Fischer P, et al. (2003) Hydrogen storage properties $LiBH_4$. *J Alloys Compd* 356–357: 515–520.
26. Smith MB, Bass GE (Jr.) (1963) Heats and Free Energies of Formation of the Alkali Aluminum Hydrides and of Cesium Hydride. *J Chem Eng Data* 8: 342–346.
27. Mauron Ph, Buchter F, Friedrichs O, et al. (2008) Stability and reversibility of $LiBH_4$. *J Phys Chem* 112: 906–910.
28. Nakamori Y, Miwa K, Ninomiya A, et al. (2006) Correlation between thermodynamical stabilities of metal borohydrides and cation electronegativities: First principle calculations and experiments. *Phys Rev B* 74: 045126 1–9.
29. Nakamori Y, Li HW, Kikuchi K, et al. (2007) Thermodynamical stabilities of metal-borohydrides. *J Alloy Compd* 446–447: 296–300.

30. Varin RA, Shirani AB (2015) Rapid, ambient temperature hydrogen generation from the solid state Li-B-Fe-H system by mechano-chemical activation synthesis. *J Power Sources* (submitted, under revision).
31. Schaeffer GW, Roscoe JS, Stewart AC (1956) The reduction of iron (III) chloride with lithium aluminohydride and lithium borohydride: iron (II) borohydride. *J Amer Chem Soc* 18: 729–733.
32. Myakishev KG, Volkov VV (2006) Mechanochemical synthesis of diborane (6) by the interaction of anhydrous chloride of iron (II), cobalt (II), nickel (II) with tetrahydroborates of alkaline metals. *Chem Suste Dev* 14: 375–378.
33. Liu XF, McGrady GS, Langmi HW, et al. (2009) Facile cycling of Ti-doped $LiAlH_4$ for high performance hydrogen storage. *J Am Chem Soc* 131: 5032–5033.
34. Liu XF, Langmi HW, Beattie SD, et al. (2011) Ti doped $LiAlH_4$ for hydrogen storage: synthesis, catalyst loading, and cyclic performance. *J Am Chem Soc* 133: 15593–15597.
35. Varin RA, Zbroniec L (2010) The effects of ball milling and nanometric nickel additive on the hydrogen desorption from lithium borohydride and manganese chloride ($3LiBH_4 + MnCl_2$) mixture. *Int J Hydrogen Energ* 35: 3588–3597.
36. Varin RA, Zbroniec L, Polanski M, et al. (2012) Mechano-chemical synthesis of manganese borohydride ($Mn(BH_4)_2$) and inverse cubic spinel (Li_2MnCl_4) in the ($nLiBH_4 + MnCl_2$) (n = 1, 2, 3, 5, 9 and 23) mixtures and their dehydrogenation behavior. *Int J Hydrogen Energ* 37: 16056–16069.
37. Varin RA, Bidabadi AS (2014) The effect of milling energy input during mechano-chemical activation synthesis (MCAS) of the nanocrystalline manganese borohydride ($Mn(BH_4)_2$) on its thermal dehydrogenation properties. *Int J Hydrogen Energ* 39: 11620–11632.
38. Černý R, Penin N, Hagemann H, et al. (2009) The first crystallographic and spectroscopic characterization of a 3d-metal borohydride: $Mn(BH_4)_2$. *J Phys Chem C* 113: 9003–9007.
39. Severa G, Hagemann H, Longhini M, et al. (2010) Thermal desorption, vibrational spectroscopic, and DFT computational studies of the complex manganese borohydrides $Mn(BH_4)_2$ and $[Mn(BH_4)_4]^{2-}$. *J Phys Chem C* 114: 15516–15521.
40. Černý R, Penin N, D'Anna V, et al. (2011) $Mg_xMn_{(1-x)}(BH_4)_2$ (x = 0–0.8), a cation solid solution in a bimetallic borohydride . *Acta Materialia* 59: 5171–5180.
41. Sandrock G, Gross K, Thomas G, et al. (2002) Engineering considerations in the use of catalyzed sodium alanates for hydrogen storage. *J Alloy Compd* 332: 696–701.
42. Sandrock G, Gross K, Thomas G (2002) Effect of Ti-catalyst content on the reversible hydrogen storage properties of the sodium alanates. *J Alloy Compd* 339: 299–308.
43. Yvon K, Lorenzoni JL (2006) Hydrogen-powered lawn mower: 14 years of operation. *Int J Hydrogen Energ* 31: 1763–1767.